

features near  $\nu = 1/2$  in optics. (2) Even if the 2DES condenses in a FQHE state and the chemical potential is located in a gap, the resonance peaks surrounding  $\nu = 1/2$  survive (Fig. 3c). Commensurability effects should not be observable in this regime. (3) Similar resonance peaks were also detected for the higher-order CFs around  $\nu = 1/4$ . As this CF metallic state is characterized by the same Fermi wavevector, GRs should occur at the same distance from  $\nu = 1/4$  as they do at  $\nu = 1/2$ . The observed peaks are located at different positions, making it difficult to support a commensurability situation (see below, and Fig. 4b).

In contrast to the electron case, the intensity of the CF cyclotron resonance is a strong nonlinear function of microwave power (Fig. 4a). Moreover, its observability only at high power correlates with the first appearance of commensurability oscillations. The drop in intensity at even higher power is probably caused by heating. The intensity diminishes to zero at temperatures above 0.7 K, whereas the electron resonance persists up to  $T > 2$  K. The slope of the CF cyclotron frequency as a function of  $B^*$  in Fig. 3c defines the cyclotron mass  $m_{\text{cf}}^{\text{cf}}$ . This mass is set by the electron–electron interaction scale, so that a square-root dependence on density or magnetic field is predicted from a straightforward dimensional analysis<sup>4</sup>. Numerical calculations predict  $m_{\text{cf}}^{\text{cf}}/m_0 = 0.079(B)^{1/2}$  for an ideal 2DES (here  $B$  is in tesla), not including Landau level mixing or finite width contributions<sup>17</sup>. The data, shown in Fig. 4b, confirm qualitatively the marked enhancement in comparison with the electron mass (more than 10 times); however, a fit to the square-root dependence requires a prefactor that is four times larger. Previously reported mass values based on measurements of the activation energy gap<sup>18,19</sup> must be distinguished from the cyclotron mass. The former corresponds to the limit of infinite momentum, whereas here  $k$  approaches zero. Moreover, activation gaps can only be extracted at well developed fractional quantum Hall states, and their accurate determination suffers from disorder-induced broadening. These and other limitations have been discussed in ref. 19. The present technique can be performed at arbitrary filling factors. □

Received 27 April; accepted 14 November 2001.

1. Das Sarma, S. & Pinczuk, A. (eds) *Perspectives on Quantum Hall Effects* (Wiley, New York, 1996).
2. Jain, J. K. The composite fermion: a quantum particle and its quantum fluids. *Physics Today* 53 (4), 39–45 (2000).
3. Jain, J. K. Composite fermion approach for the fractional quantum Hall effect. *Phys. Rev. Lett.* 63, 199–202 (1989).
4. Halperin, B. I., Lee, P. A. & Read, N. Theory of the half-filled Landau level. *Phys. Rev. B* 47, 7312–7343 (1993).
5. Heinonen, O. (ed.) *Composite Fermions* (World Scientific, Singapore, 1998).
6. Du, R. R., Stormer, H. L., Tsui, D. C., Pfeiffer, L. N. & West, K. W. Experimental evidence for new particles in the fractional quantum Hall effect. *Phys. Rev. Lett.* 70, 2944–2947 (1993).
7. Du, R. R. *et al.* Fractional quantum Hall effect around  $\nu = 3/2$ : composite fermions with a spin. *Phys. Rev. Lett.* 75, 3926–3929 (1995).
8. Willett, R. L., Ruel, R. R., West, K. W. & Pfeiffer, L. N. Experimental demonstration of a Fermi surface at one-half filling of the lowest Landau level. *Phys. Rev. Lett.* 71, 3846–3849 (1993).
9. Goldman, V. J., Su, B. & Jain, J. K. Detection of composite fermions by magnetic focusing. *Phys. Rev. Lett.* 72, 2065–2068 (1994).
10. Smet, J. H., Weiss, D., Blick, R. H., Lütjering, G. & von Klitzing, K. Magnetic focusing of composite fermions through arrays of cavities. *Phys. Rev. Lett.* 77, 2272–2275 (1996).
11. Kohn, W. Cyclotron resonance and de Haas-van Alphen oscillations of an interacting electron gas. *Phys. Rev.* 123, 1242–1244 (1961).
12. Gubarev, S. I. *et al.* Screening of excitonic states by low-density 2D charge carriers in GaAs/AlGaAs quantum wells. *JETP Lett.* 72, 324–328 (2000).
13. Allen, S. J., Stömer, H. L. & Hwang, J. C. M. Dimensional resonance of the two-dimensional electron gas in selectively doped GaAs/AlGaAs heterostructures. *Phys. Rev.* 28, 4875–4877 (1983).
14. Gerhardt, R. R., Weiss, D. & von Klitzing, K. Novel magnetoresistance oscillations in a periodically modulated two-dimensional electron gas. *Phys. Rev. Lett.* 62, 1173–1176 (1989).
15. Shilton, J. M. *et al.* Effect of spatial dispersion on acoustoelectric current in a high mobility two-dimensional electron gas. *Phys. Rev. B* 51, 14770–14773 (1995).
16. Jain, J. K. & Kamilla, R. K. in *Composite Fermions* (ed. Heinonen, O.) 1–80 (World Scientific, Singapore, 1998).
17. Park, K. & Jain, J. K. Phase diagram of the spin polarization of composite fermions and a new effective mass. *Phys. Rev. Lett.* 80, 4237–4240 (1998).
18. Du, R. R., Stormer, H. L., Tsui, D. C., Pfeiffer, L. N. & West, K. W. *Phys. Rev. Lett.* 70, 2944–2947 (1993).
19. Willett, R. L. in *Composite Fermions* (ed. Heinonen, O.) 349–431 (World Scientific, Singapore, 1998).

## Acknowledgements

We acknowledge the Volkswagen Stiftung, the Russian Fund of Fundamental Research, INTAS, the German Ministry of Science and Education and the German Physical Society for their support.

## Competing interests statement

The authors declare that they have no competing financial interests.

Correspondence and requests for materials should be addressed to J.H.S. (e-mail: jhsmet@klizix.mpi-stuttgart.mpg.de).

# Imaging the granular structure of high- $T_c$ superconductivity in underdoped $\text{Bi}_2\text{Sr}_2\text{CaCu}_2\text{O}_{8+\delta}$

K. M. Lang\*, V. Madhavan\*, J. E. Hoffman\*, E. W. Hudson\*†‡, H. Eisaki§, S. Uchida§ & J. C. Davis\*‡

\* Department of Physics, University of California, Berkeley, California 94720, USA

† Department of Physics, Massachusetts Institute of Technology, Cambridge, Massachusetts 02139-4301, USA

‡ Materials Science Division, Lawrence Berkeley National Laboratory, Berkeley, California 94720, USA

§ Department of Superconductivity, University of Tokyo, Yayoi, 2-11-16 Bunkyo, Tokyo 113-8656, Japan

|| Department of Applied Physics, Stanford University, Stanford, California 94205-4060, USA

**Granular superconductivity occurs when microscopic superconducting grains are separated by non-superconducting regions; Josephson tunnelling between the grains establishes the macroscopic superconducting state<sup>1</sup>. Although crystals of the copper oxide high-transition-temperature (high- $T_c$ ) superconductors are not granular in a structural sense, theory suggests that at low levels of hole doping the holes can become concentrated at certain locations resulting in hole-rich superconducting domains<sup>2–5</sup>. Granular superconductivity arising from tunnelling between such domains would represent a new view of the underdoped copper oxide superconductors. Here we report scanning tunnelling microscope studies of underdoped  $\text{Bi}_2\text{Sr}_2\text{CaCu}_2\text{O}_{8+\delta}$  that reveal an apparent segregation of the electronic structure into superconducting domains that are  $\sim 3$  nm in size (and local energy gap  $< 50$  meV), located in an electronically distinct background. We used scattering resonances at Ni impurity atoms<sup>6</sup> as ‘markers’ for local superconductivity<sup>7–9</sup>; no Ni resonances were detected in any region where the local energy gap  $\Delta > 50 \pm 2.5$  meV. These observations suggest that underdoped  $\text{Bi}_2\text{Sr}_2\text{CaCu}_2\text{O}_{8+\delta}$  is a mixture of two different short-range electronic orders with the long-range characteristics of a granular superconductor.**

Evidence from scanning tunnelling microscopy (STM) for nanoscale spatial variations in the electronic characteristics of  $\text{Bi}_2\text{Sr}_2\text{CaCu}_2\text{O}_{8+\delta}$  ( $\text{Bi-2212}$ ) has been steadily accumulating<sup>10–12</sup>. Recent advances include observations of nanoscale regions with ‘superconducting’ spectra coexisting with regions characterized by ‘pseudogap-like’ spectra<sup>13,14</sup>, and the observation of spatial inhomogeneities in the gap magnitude that correlate with those in integrated differential tunnelling conductance<sup>15</sup>. Several theoretical models have emerged in response to these data<sup>16–22</sup>. A frequent theme among these models is that strong electrostatic-potential variations are experienced by the itinerant holes. Such potential fluctuations could be caused by frustrated electronic phase separation<sup>2–5</sup>, by unscreened dopant atoms<sup>15,19–21</sup>, or by some other

unrelated disorder<sup>16–18,22</sup>. In any of these cases, the holes would redistribute themselves to minimize their total energy in the disordered potential landscape. At low hole densities, some regions would therefore remain doped while others would be relatively undoped. Thus, two types of electronic order—superconducting and non-superconducting respectively—would coexist in different nanoscale regions of the same crystal<sup>16–19</sup>. If Josephson tunnelling were to couple the superconducting domains, the crystal would exhibit granular superconductivity<sup>13,23</sup>.

These predictions can be explored by STM, as it can access real-space electronic structure with atomic resolution. Here we report high-resolution STM studies of underdoped Bi-2212. The samples are single crystals grown by the floating zone method. The ‘as-

grown’ samples have a hole-dopant level  $p \approx 0.18 \pm 0.02$  while the underdoped samples are oxygen-depleted with a superconducting transition temperature  $T_c$  of 79 K and  $p \approx 0.14 \pm 0.02$ . They are cleaved in cryogenic ultrahigh vacuum at  $T < 30$  K and, when inserted into the STM head, show atomic resolution on the BiO surface plane. Our primary data sets consist of differential tunnelling conductance spectra ( $dI/dV$  versus  $V$ ) measured at all locations in a given field of view. These ‘spectral surveys’ are essentially detailed spatial maps of the local density of electronic states (LDOS) as a function of energy  $E$ , because  $\text{LDOS}(E) \propto dI/dV(V)$  where  $V$  is the sample bias,  $e$  is the electron charge, and  $E = eV$ .

Spectral surveys can be analysed to yield maps of the energy gap as a function of location (‘gap maps’) by defining  $\Delta$  for each  $dI/dV$  spectrum as:

$$\Delta \equiv \frac{\Delta_+ - \Delta_-}{2} \quad (1)$$

Here  $\Delta_{+(-)}$  is the energy of the first peak above (below) the Fermi level. Peaks from scattering resonances are disregarded, and  $\Delta$  does not necessarily represent a superconducting energy gap.

In Fig. 1 we show gap maps extracted from two such spectral surveys, each measured on an area of  $560 \text{ \AA} \times 560 \text{ \AA}$ . They use an identical colour scale. Figure 1a is typical of gap maps on underdoped Bi-2212, while Fig. 1b is typical of the slightly overdoped ‘as-grown’ samples. They are very different in appearance. The as-grown gap map is dominated by large interconnected areas of low  $\Delta$  (red and yellow), interspersed with filamentary high- $\Delta$  areas (blue and black). This is in contrast to the underdoped sample in Fig. 1a in which the compact, spatially distinct, low- $\Delta$  regions (red and yellow) are surrounded by interconnected high- $\Delta$  regions (blue and black). For the as-grown sample shown, the mean gap value is  $\bar{\Delta} = 35.6$  meV with a standard deviation  $\sigma = 7.7$  meV, while for the underdoped sample shown  $\bar{\Delta} = 50$  meV and  $\sigma = 8.6$  meV. Were these gap maps the only information available, one might suspect that reducing the oxygen doping has merely shifted  $\bar{\Delta}$ . But as we show below using both additional information from the spectral surveys and new experimental techniques, the differences between as-grown and underdoped samples are more profound.

Even though the spectral surveys yielding Fig. 1 had spatial resolution of  $\approx 4 \text{ \AA}$ , the spectra can show strong variations from one pixel to the next. Therefore, an accurate description of the electronic structure requires higher-spatial-resolution spectral surveys. Figure 2a shows a typical gap map from such a high-resolution spectral survey acquired with  $128 \times 128$  pixels on the area ( $147 \text{ \AA} \times 147 \text{ \AA}$ ) indicated by the white box in Fig. 1a. Figure 2b is a map of the gap-edge peak amplitude,  $G(\Delta_-)$ , from the same spectral survey. In a conventional superconductor this would be a map of the coherence-peak heights. We use the same colour bar to represent  $\Delta$  in Fig. 2a and  $G(\Delta)$  in Fig. 2b, to illustrate the spatial correlations between these two observable parameters. In these figures we see what appear to be compact, almost circular, domains. They are characterized by a low value of  $\Delta$ , and a  $G(\Delta)$  that rises rapidly from the domain edge to reach a maximum at the domain centre. We will refer to these regions as  $\alpha$ -domains. As an example, a single  $\alpha$ -domain is identified inside the white circle on Fig. 2a and b. Different  $\alpha$ -domains have a different characteristic values of  $\Delta$ , and multiple  $\alpha$ -domains are clumped together at some locations. Intervening between the  $\alpha$ -domains are percolative regions characterized by high  $\Delta$  and low, almost-constant  $G(\Delta)$ . We will refer to these spectroscopically distinct areas as  $\beta$ -regions.

Figure 2c and d shows the evolution of  $\Delta$  and  $G(\Delta)$ , respectively, with distance along the white line in Fig. 2a and b. Within each  $\alpha$ -domain, the value of  $\Delta$  varies little, while  $G(\Delta)$  rises rapidly from the perimeter reaching a maximum in the centre. In the surrounding interconnected  $\beta$ -regions,  $\Delta$  varies slowly while  $G(\Delta)$  is low and almost constant. Figure 2 focuses on the typical evolution of  $\Delta$  and  $G(\Delta)$ , but these parameters represent only a small subset of the

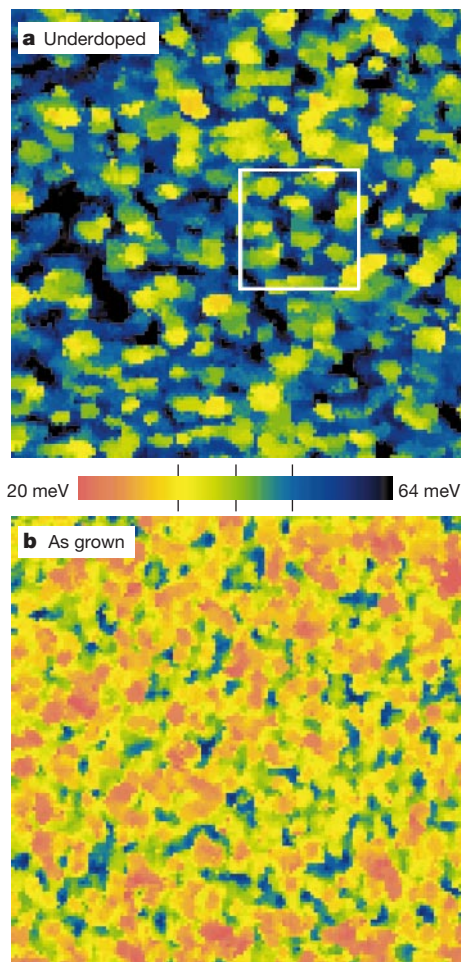


**Figure 1** Typical gap maps from underdoped and as-grown Bi-2212 samples, each showing an area of  $560 \text{ \AA} \times 560 \text{ \AA}$ . We use an identical colour scale to represent  $\Delta$  in these two panels for ease of comparison. The colour scale spans the range 20–64 meV, and ticks on the scale are placed at 34 meV, 42 meV and 50 meV. These gap maps were calculated from two  $128 \times 128$  pixel spectral surveys. **a**, Gap map of an oxygen-underdoped Bi-2212 sample with  $T_c = 79$  K. This field of view contains approximately 130 compact low- $\Delta$  domains which are visible as orange, yellow and green islands against the interconnected blue and black background which are the high- $\Delta$  regions. **b**, Gap map of an as-grown Bi-2212 sample. The interconnected red, orange and yellow low- $\Delta$  regions completely dominate the image. Embedded in this environment are filamentary blue and black high- $\Delta$  regions. Note that although this sample contains a 0.5% substitution of Ni for the Cu atoms in the  $\text{CuO}_2$  plane, the 102 impurity resonances in this field of view affect less than 15% of the area, and furthermore, the local value of  $\Delta$  does not vary near the Ni impurities<sup>6</sup>. Both spectral surveys were acquired with constant-current normalization in cryogenic ultrahigh vacuum at 4.2 K with tunnel junction resistance of  $1 \text{ G}\Omega$  set at  $V = -100$  mV.

information in a spectral survey. To see directly how the electronic phenomena reported here are manifest in the raw data, we show in Fig. 3 the unprocessed  $dI/dV$  spectra measured along the white line in Fig. 2a and b. The spectral evolution with passage through three  $\alpha$ -domains (red) and the intervening  $\beta$ -regions (blue) can be seen.

Figures 2 and 3 show how, on the basis of two observables ( $\Delta$  and  $G(\Delta)$ ), the  $\alpha$ -domains and  $\beta$ -regions appear spectroscopically distinct. We refer to this situation as electronic segregation. It becomes apparent only in underdoped samples, because  $\Delta < 50$  meV for the  $\alpha$ -domains and these samples have  $\Delta > 50$  meV for  $\sim 50\%$  of their area, while the as-grown samples studied have  $\Delta > 50$  meV for only  $\sim 10\%$  of theirs. This apparent electronic segregation motivates a new picture of the effects of reducing oxygen doping in Bi-2212. The  $\alpha$ -domains have characteristics usually associated with superconductivity—for example, sharp gap-edge peaks indicating well defined Bogoliubov quasiparticles and an increasing areal density associated with rising  $T_c$  below optimal doping. In contrast, the  $\beta$ -region spectra exhibit characteristics often associated with the pseudogap phase (although we cannot definitively identify these regions as such). Consequently, the emerging picture is reminiscent

of a granular superconductor with coupled superconducting grains embedded in a distinct electronic environment.

As STM is a surface probe, we next consider whether the observed phenomena represent a property of bulk underdoped Bi-2212. Evidence for strong nanoscale variations in the bulk electronic properties includes: (1) a low-temperature quasiparticle lifetime at least an order of magnitude shorter<sup>24</sup> in Bi-2212 than in  $\text{YBa}_2\text{Cu}_3\text{O}_{7-\delta}$ , (2) optical conductivity measurements demonstrating a finite low-temperature  $\sigma_1$  (ref. 24) that can be explained by strong nanoscale variations in local superfluid density<sup>25</sup>, (3) heat-capacity ( $\equiv C$ ) measurements showing that with underdoping,  $\gamma \equiv C/T$  falls rapidly and the temperature range of the transition widens dramatically<sup>26</sup>, (4) NMR studies showing very broad line-widths and additional spin susceptibility at low temperature indicative of strong electronic disorder<sup>27</sup>, (5) inelastic neutron scattering line-widths that are significantly wider in Bi-2212 than in other copper oxides<sup>28</sup>, (6) ARPES studies showing similar evolution of spectra with deliberately introduced bulk disorder as with underdoping<sup>29</sup>, and (7) interlayer tunnelling experiments demonstrating the co-existence of superconducting and non-supercon-

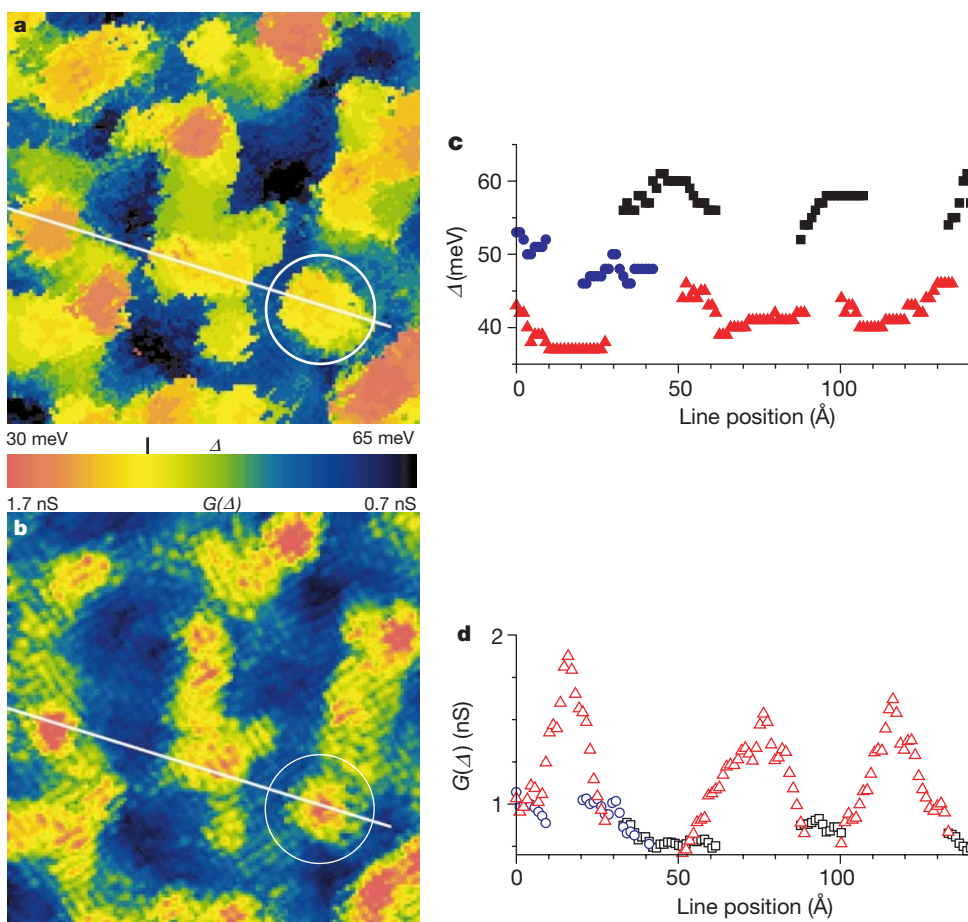


**Figure 2** Data obtained at high spatial resolution, showing the typical spatial interrelationship of  $\Delta$  and  $G(\Delta)$  for underdoped Bi-2212. These data were generated from a single  $128 \times 128$  pixel spectral survey which was taken on the  $147 \text{ \AA} \times 147 \text{ \AA}$  region inside the white box in Fig. 1a. This spectral survey was taken several weeks after the survey used to calculate Fig. 1a, during which the sample was kept continuously at 4.2 K. **a**, High-resolution gap map revealing approximately 12  $\alpha$ -domains embedded in the percolative  $\beta$ -like background. **b**, Map of  $G(\Delta)$  at the same location as **a**. Here, to reveal the spatial correlations between  $\Delta$  and  $G(\Delta)$ , we use the same colour bar as in **a** but here the scale is inverted and represents  $G(\Delta)$ . Note that  $G(\Delta)$  is defined as the gap-edge peak at negative bias throughout this Letter. In **c** we show the spatial evolution of  $\Delta$  and in **d** of  $G(\Delta)$  along the trajectory of the white line seen in **a** and **b**. Figures 2 and 3 together

illustrate the properties of the two distinct types of regions. In terms of  $\Delta$ , the  $\alpha$ -domains are defined by a distinct value of  $\Delta$  which is  $\leq 50$  meV and which is constant to 5% within a 13- $\text{\AA}$  radius of the centre of each domain, while the  $\beta$ -regions are defined by  $\Delta \geq 35$  meV. There exists an overlap range of  $\Delta$  ( $35 \text{ meV} \leq \Delta \leq 50 \text{ meV}$ ) in which categorization must rely on parameters in addition to  $\Delta$ . The tick mark on the colour scale is at 42 meV at the centre of this overlap range. In terms of  $G(\Delta)$ , the  $\alpha$ -domains are defined by  $G(\Delta)$  at the centre of the domain being  $\sim 66\%$  ( $\sigma = 23\%$ ) above the average  $\beta$ -region  $G(\Delta)$ , which itself has  $\sigma = 15\%$ . Similar conclusions are derived from all equivalent maps from other underdoped spectral surveys. The spectral survey was acquired with constant current normalization at 4.2 K with tunnel junction resistance of 1  $\text{G}\Omega$  set at  $V = -200$  mV.

ducting energy gaps<sup>30,31</sup>. Results from these different techniques would be consistent with each other and with STM data if nanoscale variations exist in the properties of bulk Bi-2212, and if they are amplified by underdoping.

Although the data in Figs 1–3 suggest granular superconductivity, single-particle excitation spectra cannot definitively distinguish between such superconductivity and a highly disordered single-phase superconductor. However, a novel atomic-scale technique, designed to locally distinguish superconducting from non-superconducting regions by using quasiparticle scattering resonances at Ni impurity atoms, has recently been proposed<sup>7–9</sup>. A scattering resonance originates from interactions between quasiparticles and an impurity atom, and appears as an additional peak (or peaks) in the excitation spectrum near the impurity. Ni scattering resonances are particle–hole symmetric in the superconducting state<sup>6</sup>, are predicted to lose this symmetry if an electronic ‘pseudogap’ is present<sup>8,9</sup>, and might disappear completely if conventional quasiparticles are non-existent<sup>7</sup>. Thus, study of Ni scattering resonances as a function of local  $\Delta$  should, in theory, allow the discrimination of superconducting from non-superconducting regions.

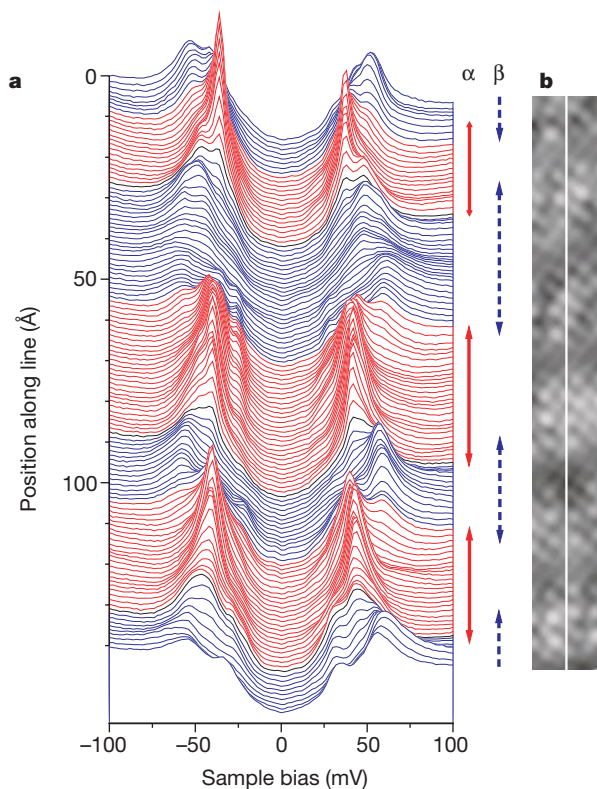


**Figure 3** Typical series of  $dI/dV$  spectra illustrating how the two distinct types of regions are apparent in the raw data. **a**, These unprocessed spectra were extracted from the same spectral survey used to create Fig. 2, along the white line shown in Fig. 2a and b. The spectra are separated by 1.1 Å and span a total distance of 140 Å as represented by their vertical offset. The  $\alpha$ -domain spectra (red) have low gap magnitudes and sharp gap-edge peaks whose amplitude is low at the edges of the domain and rises to a maximum in the centre. The  $\beta$ -region spectra have high gap magnitude and very broad gap-edge peaks whose amplitude is relatively low and constant. Additional features seen in this figure are the spectra that lie on the borders between neighbouring distinct regions. These spectra can show four peaks, where each pair of peaks corresponds to the gap value of the neighbouring regions. For the maps shown in Figs 1 and 2, the peak with the overall maximum value of  $G(eV)$  is used to determine  $\Delta$  and  $G(\Delta)$ . In Fig. 2c and d, if four clear peaks can be identified in the  $dI/dV$  spectrum, then both values of  $\Delta$  and  $G(\Delta)$  at that location are plotted. **b**, Surface topography with the trajectory along which both the spectra in **a**, and the traces of Fig. 2c and d, were measured, shown as a white line. The atomic resolution associated with the spectral surveys is clearly evident.

We apply this technique by carrying out spectral surveys on as-grown Ni-doped Bi-2212 samples. Figure 4 summarizes results from two such experiments. Figure 4a shows the positions of the Ni scattering resonances (which are identified by their strongest resonance peak near +18 meV; ref. 6) superimposed on the gap map derived from the same spectral survey. The colour scale is such that regions with  $\Delta < 50$  meV (light grey) are distinguished from those with  $\Delta > 50$  meV (dark grey). No Ni scattering resonances are observed in any region where  $\Delta > 50 \pm 2.5$  meV. To clarify the correlation between Ni resonances and  $\Delta$ , we plot in Fig. 4b a combined histogram (shown red) of observed Ni resonances versus local  $\Delta$  from two independent spectral surveys on different crystals. The combined histogram of  $\Delta$  from the same two spectral surveys is shown in grey. Although for  $\Delta < 35$  meV the two distributions are similar in shape, above  $\Delta \approx 35$  meV they rapidly diverge and the Ni-resonance distribution reaches zero by 50 meV.

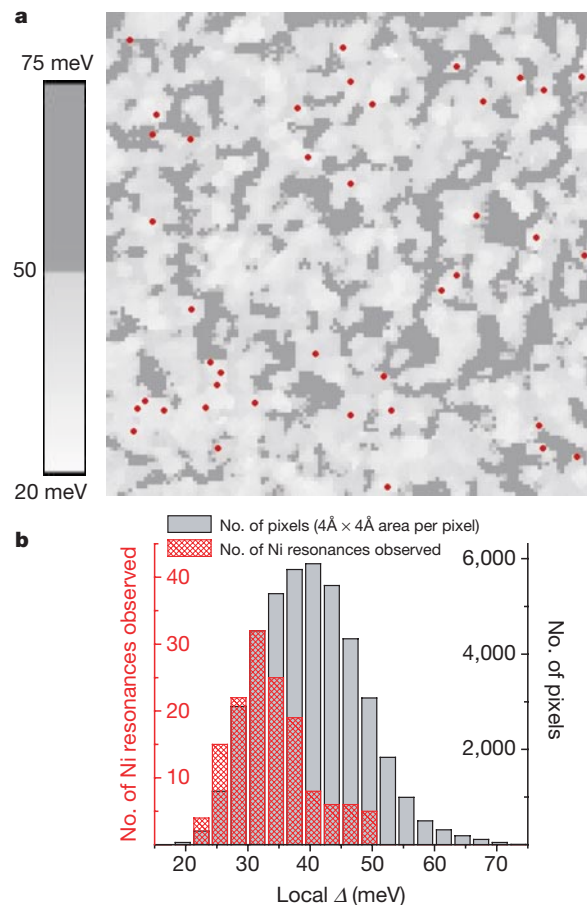


**Figure 4** Analysis of the relationship between Ni scattering resonances and local  $\Delta$ . Spectral surveys were acquired at 4.2 K on two as-grown Ni-doped Bi-2212 samples, both with tunnel junction resistance of 1 G $\Omega$  set at  $V = -100$  mV. Using the +18 mV LDOS image of each survey, the locations of Ni resonances were identified by the strong resonance peak at +18 mV in their  $dI/dV$  spectra<sup>6</sup>. For  $\approx 30\%$  of these resonances, the full particle–hole symmetric signature (spatial and spectroscopic) of a Ni resonance<sup>6</sup> was directly confirmed. The location of the Ni resonances can be correlated with the local value of  $\Delta$  extracted from these same two surveys. **a**, The location of the Ni resonances (red dots) superimposed on the simultaneously acquired gap map of an area 600 Å  $\times$  600 Å. No Ni resonances are observed in regions where  $\Delta > 50$  meV. **b**, Histograms derived from a combined analysis of the above spectral survey on 0.2% Ni-doped Bi-2212, and an independent 568 Å  $\times$  568 Å survey on 0.5% Ni-doped Bi-2212. For each Ni resonance, the local  $\Delta$  is determined by the spatial average of  $\Delta$  over a 13 Å square region centred on the impurity. Using this information, we plot in red a combined histogram of observed Ni resonances versus  $\Delta$  from both samples. The combined histogram of  $\Delta$  from the same two surveys is shown in grey.

There are several possible explanations for the Ni-resonance distribution. First, the amplitude of the 18-meV resonance peak might fall with rising  $\Delta$  and disappear near  $\Delta \approx 50$  meV. However, measurement of the peak heights shows them to be almost independent of local  $\Delta$ . Second, there might be statistical fluctuations such that no Ni atoms reside in regions where  $\Delta > 50$  meV. However, if the Ni atoms are distributed randomly, and if all regions can support quasiparticle scattering resonances, our non-observation (in two independent experiments on different crystals) of Ni resonances in regions with  $\Delta > 50$  meV has a combined probability of no more than  $3 \times 10^{-5}$ . Therefore this explanation also appears to be ruled out. A third explanation could be that the Ni atoms somehow 'seed' nanoscale regions (perhaps by attracting the dopant oxygen atoms or the holes), influencing them to develop into superconducting domains with  $\Delta < 50$  meV. This model seems unlikely because, in one Zn-doped sample studied, Zn impurity resonances disappear in a statistically similar fashion near  $\Delta \sim 50$  meV—but it cannot be ruled out. Nevertheless, impurity atoms are clearly not necessary to create  $\alpha$ -domains as they exist in samples with no impurity atoms (see Figs 1a, 2 and 3).

A final hypothesis is that Ni impurity atoms are in fact physically present in regions with  $\Delta > 50$  meV, but that they do not create scattering resonances because these regions represent an electronically distinct phase. If Ni atoms are randomly distributed, and if the locations of particle-hole symmetric Ni resonances indicate the local existence of superconductivity, then the distribution of superconducting regions has a similar shape to the red histogram of Fig. 4b. The picture would then be of purely superconducting regions when  $\Delta \lesssim 35$  meV, a mixture of two different electronic orders when  $35 \text{ meV} \lesssim \Delta \lesssim 50$  meV, and an unidentified second phase (possibly the pseudogap) when  $\Delta \gtrsim 50$  meV. The data in Figs 1–3 corroborate this picture, particularly because the energy where the superconducting  $\alpha$ -domains disappear is very close to the energy where the Ni resonances disappear. Therefore, although we cannot distinguish between the possible microscopic mechanisms<sup>2,4,5,15–22</sup> for the phenomena reported here, the data all suggest that underdoped Bi-2212 is a granular superconductor. This provides a new and unconventional context in which to view the underdoped copper oxides. □

Received 28 August; accepted 4 December 2001.

1. Simánek, E. *Inhomogeneous Superconductors: Granular and Quantum Effects* (Oxford Univ. Press, New York, 1994).
2. Gor'kov, L. P. & Sokol, A. V. Phase stratification of an electron liquid in the new superconductors. *JETP Lett.* **46**, 420–423 (1987).
3. Zaanen, J. & Gunnarsson, O. Charge magnetic domain lines and the magnetism of high- $T_c$  oxides. *Phys. Rev. B* **40**, 7391–7394 (1989).
4. Emery, V. J., Kivelson, S. A. & Lin, H. Q. Phase separation in the t-J model. *Phys. Rev. Lett.* **64**, 475–478 (1990).
5. Emery, V. J. & Kivelson, S. A. Frustrated electronic phase separation and high-temperature superconductors. *Physica C* **209**, 597–621 (1993).
6. Hudson, E. W. *et al.* Interplay of magnetism and high- $T_c$  superconductivity at individual Ni impurity atoms in  $\text{Bi}_2\text{Sr}_2\text{CaCu}_2\text{O}_{8+\delta}$ . *Nature* **411**, 920–924 (2001).
7. Flatté, M. E. Nickel probes superconductivity. *Nature* **411**, 901–903 (2001).
8. Flatté, M. E. Quasiparticle resonant states as a probe of short-range electronic structure and Andreev coherence. *Phys. Rev. B* **61**, R14920–R14923 (2000).
9. Kruijs, H. V., Martin, I. & Balatsky, A. V. Impurity-induced resonant state in a pseudogap state of a high- $T_c$  superconductor. *Phys. Rev. B* **64**, 054501–1–054501–4 (2001).
10. Liu, J.-X., Wan, J.-C., Goldman, A. M., Chang, Y. C. & Jiang, P. Z. Features of the density of states of high- $T_c$  superconductors probed by vacuum tunneling. *Phys. Rev. Lett.* **67**, 2195–2198 (1991).
11. Chang, A., Rong, Z. Y., Ivanchenko, Y. M., Lu, F. & Wolf, E. L. Observation of large tunneling-conductance variations in direct mapping of the energy gap of single-crystal  $\text{Bi}_2\text{Sr}_2\text{CaCu}_2\text{O}_{8-x}$ . *Phys. Rev. B* **46**, 5692–5698 (1992).
12. Cren, T. *et al.* Influence of disorder on the local density of states in high- $T_c$  superconducting thin films. *Phys. Rev. Lett.* **84**, 147–150 (2000).
13. Howald, C., Fournier, P. & Kapitulnik, A. Inherent inhomogeneities in tunneling spectra of  $\text{Bi}_2\text{Sr}_2\text{CaCu}_2\text{O}_{8-x}$  crystals in the superconducting state. *Phys. Rev. B* **64**, 100504–1–100504–4 (2001).
14. Cren, T., Rodichev, D., Sacks, W. & Klein, J. Nanometer scale mapping of the density of states in an inhomogeneous superconductor. *Europhys. Lett.* **54**, 84–90 (2001).
15. Pan, S. H. *et al.* Microscopic electronic inhomogeneity in the high- $T_c$  superconductor  $\text{Bi}_2\text{Sr}_2\text{CaCu}_2\text{O}_{8+x}$ . *Nature* **413**, 282–285 (2001).
16. Ovchinnikov, Y. N., Wolf, S. A. & Kresin, V. Z. Intrinsic inhomogeneities in superconductors and the pseudogap phenomenon. *Phys. Rev. B* **63**, 064524–1–064524–6 (2001).

17. Ghosal, A., Randeria, M. & Trivedi, N. Inhomogeneous pairing in highly disordered s-wave superconductors. *Phys. Rev. B* **65**, 014501–1–014501–13 (2002).
18. Burgly, J., Mayr, M., Martin-Mayor, V., Moreo, A. & Dagotta, E. Colossal effects in transition metal oxides caused by intrinsic inhomogeneities. *Phys. Rev. Lett.* **87**, 277202–1–277202–4 (2001).
19. Wang, Z., Engelbrecht, J. R., Wang, S., Ding, H. & Pan, S. H. Inhomogeneous d-wave superconducting state of a doped Mott insulator. Preprint cond-mat/0107004 at (<http://xxx.lanl.gov>) (2001); *Phys. Rev. B* **65**, (2002) (in the press).
20. Martin, I. & Balatsky, A. V. Doping-induced inhomogeneity in high- $T_c$  superconductors. *Physica C* **357–360**, 46–48 (2001).
21. Wang, Q.-H., Han, J. H. & Lee, D.-H. Pairing near the Mott insulating limit. *Phys. Rev. B* **65**, 054501–1–054501–4 (2002).
22. Phillips, J. C. & Jung, J. Nanodomain structure and function of high-temperature superconductors. *Phil. Mag.* **B 81**, 745–756 (2001).
23. Deutscher, G. & Müller, K. A. Origin of superconductive glassy state and extrinsic critical currents in high- $T_c$  oxides. *Phys. Rev. Lett.* **59**, 1745–1747 (1987).
24. Corson, J., Orenstein, J., Oh, S., O'Donnell, J. & Eckstein, J. N. Nodal quasiparticle lifetime in the superconducting state of  $\text{Bi}_2\text{Sr}_2\text{CaCu}_2\text{O}_{8+\delta}$ . *Phys. Rev. Lett.* **85**, 2569–2572 (2000).
25. Barabash, S., Stroud, D. & Hwang, I.-J. Conductivity due to classical phase fluctuations in a model for high- $T_c$  superconductors. *Phys. Rev. B* **61**, R14924–R14927 (2000).
26. Loram, J. W., Luo, J. L., Cooper, J. R., Liang, W. Y. & Tallon, J. L. The condensation energy and pseudogap energy scale of  $\text{Bi}_2\text{2212}$  from the electronic specific heat. *Physica C* **341–348**, 831–834 (2000).
27. Takigawa, M. & Mitzi, D. B. NMR studies of spin excitations in superconducting  $\text{Bi}_2\text{Sr}_2\text{CaCu}_2\text{O}_{8+x}$  single crystals. *Phys. Rev. Lett.* **73**, 1287–1290 (1994).
28. Fong, H. F. *et al.* Neutron scattering from magnetic excitations in  $\text{Bi}_2\text{Sr}_2\text{CaCu}_2\text{O}_{8+x}$ . *Nature* **398**, 588–591 (1999).
29. Vobornik, I. *et al.* Alternative pseudogap scenario: Spectroscopic analogies between underdoped and disordered  $\text{Bi}_2\text{Sr}_2\text{CaCu}_2\text{O}_{8+x}$ . *Phys. Rev. B* **61**, 11248–11250 (2000).
30. Krasnov, V. M., Kovalev, A. E., Yurgens, A. & Winkler, D. Magnetic field dependence of the superconducting gap and the pseudogap in  $\text{Bi}_2\text{2212}$  and  $\text{HgBr}_2\text{-Bi}_2\text{2212}$ , studied by intrinsic tunneling spectroscopy. *Phys. Rev. Lett.* **86**, 2657–2660 (2001).
31. Suzuki, M. & Watanabe, T. Discriminating the superconducting gap from the pseudogap in  $\text{Bi}_2\text{Sr}_2\text{CaCu}_2\text{O}_{8+x}$  by interlayer tunneling spectroscopy. *Phys. Rev. Lett.* **85**, 4787–4790 (2000).

**Acknowledgements**

We thank A. V. Balatsky, E. Dagotto, M. E. Flatté, S. A. Kivelson, V. Z. Kresin, R. B. Laughlin, J. W. Loram, D.-H. Lee, P. A. Lee, I. Martin, D. K. Morr, S. H. Pan, D. Pines, D. J. Scalapino, Z.-X. Shen, N. Trivedi and S. A. Wolf for discussions and communications. This work was supported by the LDRD program of Lawrence Berkeley National Laboratory, by the ONR, by the CULAR program of Los Alamos National Laboratory, by the Miller Research Foundation (J.C.D.), by IBM (K.M.L.), by Grant-in-Aid for Scientific Research, by a COE grant from the Ministry of Education, and by an International Joint Research Grant from NEDO (Japan).

Correspondence and requests for materials should be addressed to J.C.D. (e-mail: jcdavis@socrates.berkeley.edu).

.....  
**Nitrogen loss from unpolluted South American forests mainly via dissolved organic compounds**

**Steven S. Perakis\*† & Lars O. Hedin\*†**

\* *Department of Ecology and Evolutionary Biology, Corson Hall, Cornell University, Ithaca, New York 14853, USA*

.....  
**Conceptual<sup>1–4</sup> and numerical<sup>5–8</sup> models of nitrogen cycling in temperate forests assume that nitrogen is lost from these ecosystems predominantly by way of inorganic forms, such as nitrate and ammonium ions. Of these, nitrate is thought to be particularly mobile, being responsible for nitrogen loss to deep soil and stream waters. But human activities—such as fossil fuel combustion, fertilizer production and land-use change—have substantially altered the nitrogen cycle over large regions<sup>9</sup>, making it difficult to separate natural aspects of nitrogen cycling from those**

† Present addresses: US Geological Survey, Forest and Rangeland Ecosystem Science Center, 3200 SW Jefferson Way, Corvallis, Oregon 97331, USA (S.S.P.); Department of Ecology and Evolutionary Biology, and Princeton Environmental Institute, Guyot Hall, Princeton University, Princeton, New Jersey 08544, USA (L.O.H.).